

Multi-technique investigation of Ni-doped ZnO thin films on sapphire by metalorganic chemical vapor deposition

Cite as: J. Vac. Sci. Technol. A **39**, 023408 (2021); <https://doi.org/10.1116/6.0000816>

Submitted: 24 November 2020 • Accepted: 19 January 2021 • Published Online: 05 February 2021

Jiwei Chen, Jiabin Wang, Vishal Saravade, et al.



View Online



Export Citation



CrossMark

ARTICLES YOU MAY BE INTERESTED IN

[A comprehensive review of ZnO materials and devices](#)

Journal of Applied Physics **98**, 041301 (2005); <https://doi.org/10.1063/1.1992666>


[Annealing effect on the property of ultraviolet and green emissions of ZnO thin films](#)

Journal of Applied Physics **95**, 1246 (2004); <https://doi.org/10.1063/1.1633343>


[Green luminescent center in undoped zinc oxide films deposited on silicon substrates](#)

Applied Physics Letters **79**, 943 (2001); <https://doi.org/10.1063/1.1394173>





HIDEN
ANALYTICAL



40 YEARS
1982 - 2022

Instruments for Advanced Science

- Knowledge,
- Experience,
- Expertise

Click to view our product catalogue

Contact Hiden Analytical for further details:
www.HidenAnalytical.com
info@hideninc.com

Gas Analysis

- ▶ dynamic measurement of reaction gas streams
- ▶ catalysis and thermal analysis
- ▶ molecular beam studies
- ▶ dissolved species probes
- ▶ fermentation, environmental and ecological studies

Surface Science

- ▶ UHVTPD
- ▶ SIMS
- ▶ end point detection in ion beam etch
- ▶ elemental imaging - surface mapping

Plasma Diagnostics

- ▶ plasma source characterization
- ▶ etch and deposition process reaction kinetic studies
- ▶ analysis of neutral and radical species

Vacuum Analysis

- ▶ partial pressure measurement and control of process gases
- ▶ reactive sputter process control
- ▶ vacuum diagnostics
- ▶ vacuum coating process monitoring

Multi-technique investigation of Ni-doped ZnO thin films on sapphire by metalorganic chemical vapor deposition

Cite as: J. Vac. Sci. Technol. A 39, 023408 (2021); doi: 10.1116/6.0000816

Submitted: 24 November 2020 · Accepted: 19 January 2021 ·

Published Online: 5 February 2021



Jiwei Chen,^{1,2,3} Jiabin Wang,¹ Vishal Saravade,⁴ Ian T. Ferguson,⁵ Weiguo Hu,^{1,2} Zhe Chuan Feng,^{1,3,a)} and Lingyu Wan^{1,3,b)}

AFFILIATIONS

¹Center of Nano-Energy, Laboratory of Optoelectronic Materials & Detection Technology, Guangxi Key Laboratory for Relativistic Astrophysics, School of Physical Science and Technology, Guangxi University, Nanning 530004, China

²Beijing Institute of Nanoenergy and Nanosystems, Chinese Academy of Sciences, Beijing 100083, China

³State Key Laboratory of Luminescence and Applications, Changchun Institute of Optics, Fine Mechanics and Physics, Chinese Academy of Sciences, Changchun 130033, China

⁴Department of Electrical and Computer Engineering, Missouri University of Science and Technology, Rolla, Missouri 65401

⁵Southern Polytechnic College of Engineering and Engineering Technology, Kennesaw University, Kennesaw, Georgia 30144

^{a)}Present address: Science Exploring Lab, Lawrenceville, Georgia 30043; electronic addresses: zcfeng@ntu.edu.tw and fengzhechuan@gmail.com

^{b)}Electronic mail: lyw2017@gxu.edu.cn

ABSTRACT

Optical and material properties of nickel-doped zinc oxide (ZnO-Ni) grown by metalorganic chemical vapor deposition with varying Ni source flow rates are investigated. ZnO-Ni showed a good crystal quality with (002) orientation but deteriorated at high Ni source flow rates. Photoluminescence responses show a reduction in the bandgap of ZnO-Ni with an increase in the Ni source flow and also with an increase in the temperature. Ni-doping can enhance luminescences at low concentrations (<25 SCCM and ~2%) and suppress at high concentrations. Ni-related defects occur more toward the surface than bulk of the thin films. Longitudinal optical phonon replicas named 1LO and 2LO red-shifts at low Ni source flow rates ≤ 100 SCCM with an increase in the temperature from 14 to 300 K, but exhibits an “S-shaped” red-blue-red shift with a dip at 50 K at higher Ni source flow rates (150 SCCM). Ni-doping also induces asymmetric crystal vibrations and rougher surfaces with the Ni incorporation. This study enhances the understanding of Ni-doped ZnO that is needed to apply transition-metal doped ZnO for various optoelectronic applications.

Published under license by AVS. <https://doi.org/10.1116/6.0000816>

I. INTRODUCTION

Transition metal doping of semiconductor materials has attracted extensive attention in recent years to expand their optical, structural, magnetic, and thermal functionalities applicable in the fields of spintronics, thermoelectrics, and photovoltaics.^{1–3} Zinc oxide (ZnO), as a wide bandgap (3.37 eV at room temperature) semiconductor material with advantages of abundant source of raw materials, high operating temperature,⁴ and high exciton binding energy (60 meV), has been the focus in recent research studies.^{5,6}

Various metal doped ZnO have also been extensively studied.^{7–15} Nickel (in an Ni^{2+} state or similar) could be an effective transition metal dopant and could introduce energy states in the band structure of ZnO and induce magnetic properties conducive for room temperature (RT) spintronics.^{16–18} A considerable amount of research has been driven toward the understanding of magnetic, luminescent, catalytic, and electrical properties of Ni-doped ZnO.^{19–21} Abinaya *et al.* reported that as per cyclic voltammetry characteristics of both pure ZnO and Ni-doped ZnO synthesized by both facile co-precipitation (CPM) and hydro-thermal (HTM)

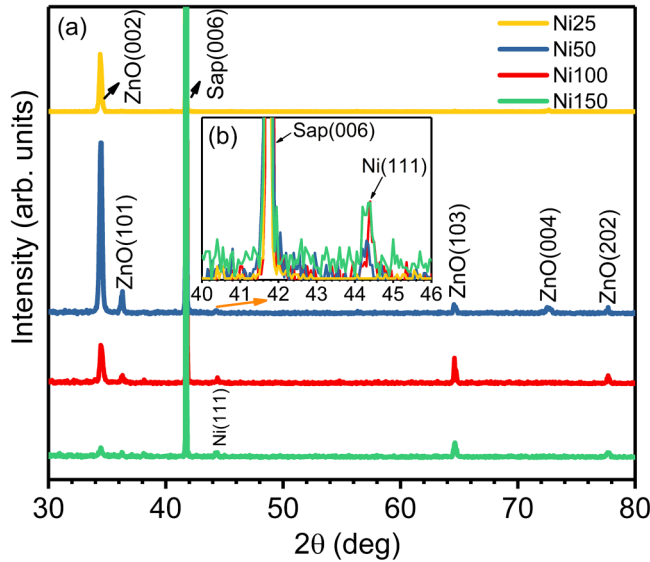


FIG. 1. (a) HRXRD 2θ - ω patterns of ZnO-Ni (peaks are identified based on host materials as Ni is doped in dilute amounts in ZnO); inset (b) is the enlarged view of the diffraction peak of the Ni phase.

methods, and the capacitive current of Ni/ZnO (HTM) reaches 12 times of pure ZnO (CPM and HTM).²² Xu *et al.* observed that, with increasing Ni composition, Ni-doped ZnO exhibits diamagnetic-ferromagnetic-paramagnetic transition.²³ Senapati *et al.* investigated catalytic performance of dilute magnetic ZnO.²⁴ Chithira and Theresa studied the Ni²⁺ doping for defect control and luminescence.²⁵ These works are significant for understanding the effect of

Ni doping on the electrical, magnetic, and optical properties of ZnO. However, regulating the concentration, morphology, and position of Ni doped in the ZnO lattice is still challenging.^{26–28} The optimal growth and performance control of nickel doping in zinc oxide still require a further penetrative investigation.

In this work, a series of ZnO films were grown at varying flow rates of the Ni source by the metal organic chemical vapor deposition (MOCVD) growth method. Crystal structures, optical properties, and phonon modes of the samples are systematically studied by means of high-resolution x-ray diffraction (HRXRD), two different wavelengths and temperature-dependent photoluminescence (TD-PL), Raman scattering, atomic force microscope (AFM), and x-ray photoelectron spectroscopy (XPS).

II. EXPERIMENT

Zinc nickel oxide (ZnO-Ni) thin films with an average thickness of 125 nm were grown on sapphire c-plane (0001) substrates by MOCVD. Diethylzinc (DEZn), oxygen (O₂), and bis (cyclopentadienyl) nickel (Cp₂Ni) were the sources for Zn, O, and Ni, respectively. Nitrogen (N₂) was used as a carrier gas. Bubbler temperatures of DEZn and Cp₂Ni were maintained at 5 and 90 °C, respectively, to adequately vaporize the sources into the reaction chamber. The films were deposited at a growth temperature of 550 °C and a chamber pressure of 2 kPa. Flow rates of DEZn and O₂ were maintained at 75 and 500 SCCM, respectively, and only the flow rate of Cp₂Ni was varied at 25, 50, 100, and 150 SCCM. The samples are named as Ni25, Ni50, Ni100, and Ni150 corresponding to the Cp₂Ni flow rates.

HRXRD (Bruker D8 Discover) was used to study the crystal structures and quality of samples. Using the Cu_{Kα} radiation ($\lambda = 1.5406 \text{ \AA}$), typical ω - 2θ patterns were acquired at

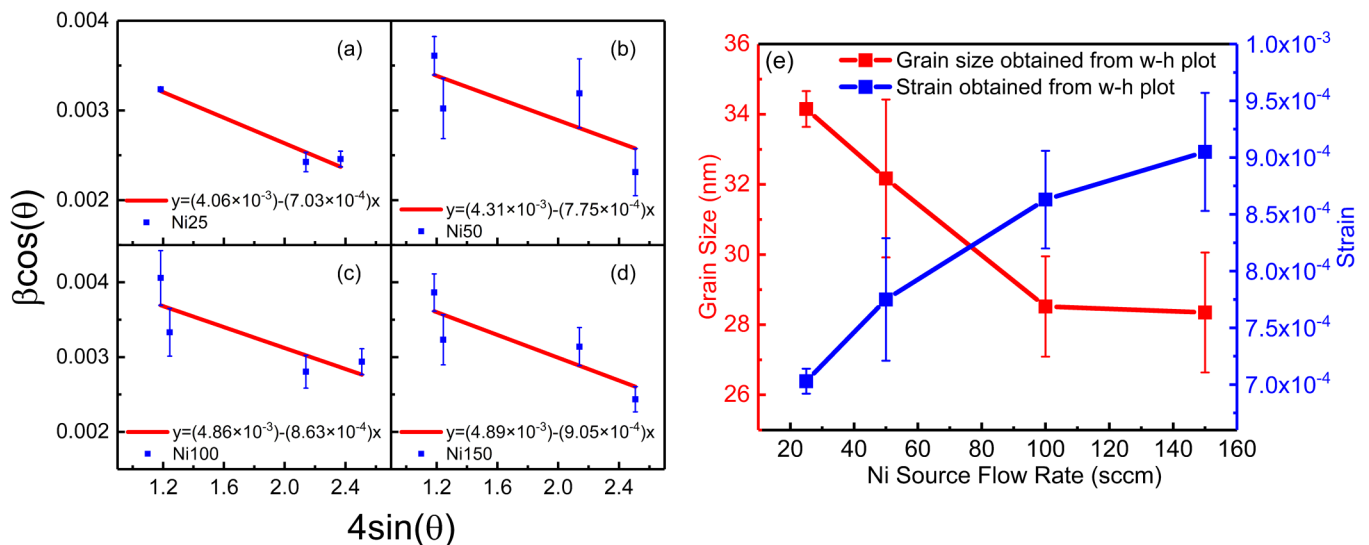


FIG. 2. (a)–(d) Williamson–Hall plots of (a) Ni25, (b) Ni50, (c) Ni100, (d) Ni(150), and (e) variations of grain size and strain estimates for all ZnO-Ni samples.

TABLE I. Structural parameters of ZnO-Ni by the Williamson–Hall method. The error estimates were obtained by 95% confidence level.

Samples	D grain size (nm)	$\epsilon \times 10^{-4}$ strain
Ni25	34.15 ± 0.51	7.03 ± 0.11
Ni50	32.17 ± 2.25	7.75 ± 0.54
Ni100	28.52 ± 1.43	8.63 ± 0.43
Ni150	28.35 ± 1.71	9.05 ± 0.52

$2\theta = 30^\circ\text{--}80^\circ$ with a step size of 0.05° . The (006) peak of the substrate and peaks of the epitaxially grown ZnO-Ni films are usually expected in this range. RT photoluminescence (RT-PL) spectra were obtained. Two sets of RT-PL measurement were

conducted, one with an excitation with of 325 nm (He-Cd laser, IK3083R-D) and another with 266 nm (FQCW266-50). These two laser sources would have different penetration depths in the thin films. TD-PL spectra were excited by a 266 nm laser (MPL-N-266) from 14 to 300 K. The temperature interval below 100 K was 10 K, between 100 and 200 K was 30 K, and above 200 K was 50 K. 325 nm laser-excited Raman spectra (Finder One laser confocal micro-Raman system) of ZnO-Ni were measured at RT. By an AFM (Dimension Icon), the surface roughness of the ZnO-Ni samples in the tapping mode was characterized. The Ni content was determined by an XPS (ESALAB 250XI⁺) system at vacuum conditions ($<5 \times 10^{-10}$ Mbar). The excitation source used was Al K α (1500 eV) radiation with an energy step size of 0.05 eV. All binding energies were calibrated by the C1s peak at 284.6 eV.

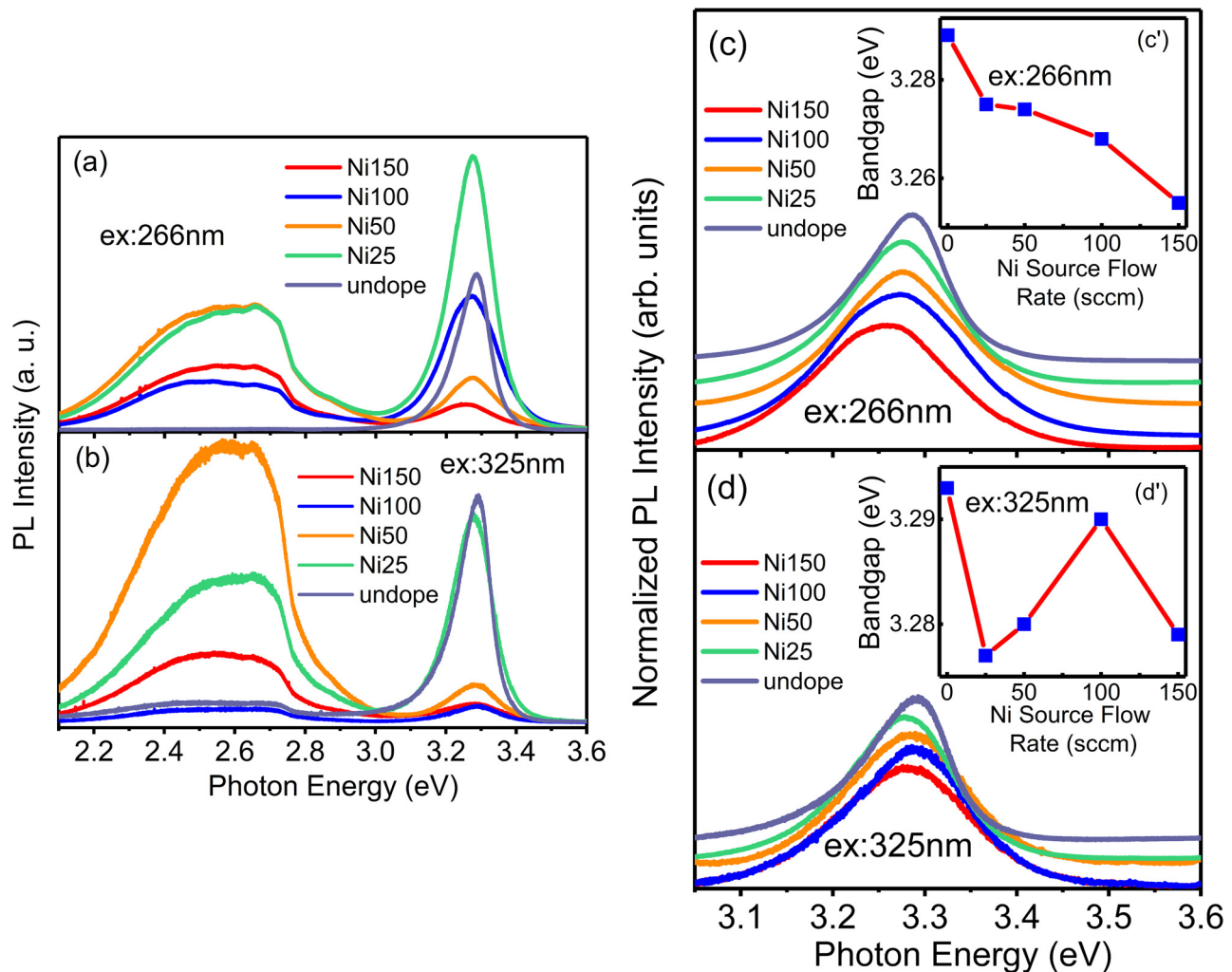


FIG. 3. PL spectra of ZnO and ZnO-Ni samples, (a) excited by 266 nm wavelength laser and (b) excited by 325 nm wavelength laser; (c) bandgap enlarged view of Figs. 3(a)–3(d). Bandgap enlarged view of Fig. 3(b); insets c' and d' show the PL bandgap changes excited by 266 nm and 325 nm wavelength laser, respectively.

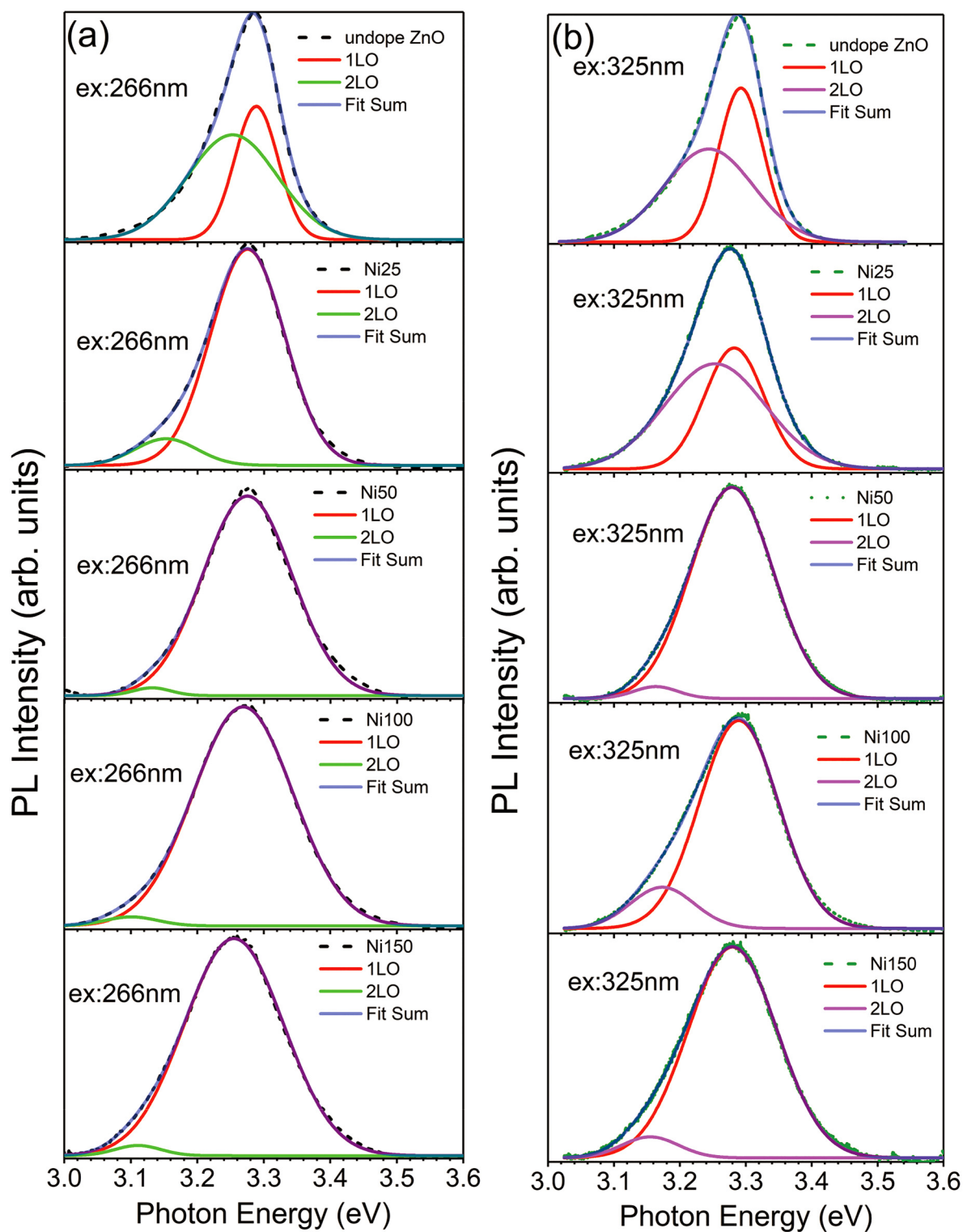


FIG. 4. Gaussian fittings of PL spectra for ZnO-Ni samples, (a) excited by 266 nm wavelength laser and (b) excited by 325 nm wavelength laser.

III. RESULTS AND DISCUSSION

A. Structural characterization of ZnO-Ni

X-ray diffraction measurement is an effective way to study the crystal structure and quality, and to identify secondary phases in the MOCVD-grown ZnO-Ni samples. Figure 1 shows the HRXRD patterns of samples grown at varying nickel source flow rates. Sap (006) is the diffraction peak of the c-plane sapphire substrate. (002) is the primary diffraction peak from ZnO-Ni with the highest diffraction intensity, which defines the wurtzite crystal structure and preferred crystal orientation in ZnO-Ni. Other ZnO (101), (103), (004), (202) secondary crystal planes were also observed (JCPDS No. 01-080-0075).²¹ ZnO-Ni shows a good crystal quality but degrades with an increase in the Ni source flow rate over ~100 SCCM. As shown in the inset of Fig. 1, samples with an Ni source flow rate above 25 SCCM contained a secondary nickel (111) phase (JCPDS No. 04-0850),²⁴ while sample with a low nickel source flow rate of 25 SCCM exhibited only ZnO-like crystal structures. Ni-related phases are formed in ZnO-Ni as the nickel source flow rate exceeds ~50 SCCM.

In XRD patterns, the half-widths of diffraction peaks are usually determined in three parts, that is, grain size, lattice distortion (defect), and instrument broadening. In order to accurately calculate the relevant parameters of the sample from the half-peak width, instrument broadening was calibrated with a standard Si sample (a function of scattering angle). Full width at half maxima [FWHM (2 θ) or β] after calibration is given by the following formula:²⁹

$$\beta = (\beta_m^2 - \beta_i^2)^{\frac{1}{2}}, \quad (1)$$

where β_m is the measured half peak width and β_i is the instrument broadening calibrated by Si.

After calibrating the effects of the instrument on the half-peak width, Williamson-Hall plots were used to estimate the sample grain size and strain.^{30,31} In this process, diffraction peak broadening is calculated by

$$\beta = \beta_s + \beta_g = 4\epsilon \tan \theta + \frac{k\lambda}{D \cos \theta}, \quad (2)$$

where β_s is the strain-induced broadening, β_g is the grain size induced broadening, ϵ is the strain, D is the grain size (diameter), K is a fixed parameter (film = 0.9), λ is the diffraction wavelength ($\text{Cu}_{K\alpha} = 0.15406 \text{ nm}$), and θ is the diffraction angle. Multiplying throughout by $\cos \theta$ gives Eq. (3),

$$\beta \cos \theta = 4\epsilon \sin \theta + \frac{k\lambda}{D}. \quad (3)$$

According to the above formulas, FWHM-related data of diffraction peaks in the (002) orientation were extracted. In plots with $4\sin \theta$ as the x axis and $\beta \cos \theta$ as the y axis, linearity fits were made as shown in Figs. 2(a)–2(d). y-intercept $y = k\lambda/D$ is the grain size D , while slope ϵ of the linear fit is an estimated strain.

The linear fitting yields a negative slope due to the compressive stress of the crystal lattice.³¹ This implies that the Ni element exists between the crystal lattices and squeezes the ZnO crystal lattice. Grain size of un-doped ZnO has a wide range from a few to hundreds of nanometers. This would depend on the growth parameters and sources used for the material's growth. In this work, the focus has been on investigating the effects of nickel doping. With Ni incorporation, the grain size is estimated to increase at least until dilute amounts of Ni. In very dilute amounts, Ni could potentially passivate intrinsic defects of ZnO and increase the grain size.^{16,32} As the Ni source flow rate increases, the grain size reduces and lattice strain increases as shown in Fig. 2(e). This shows the

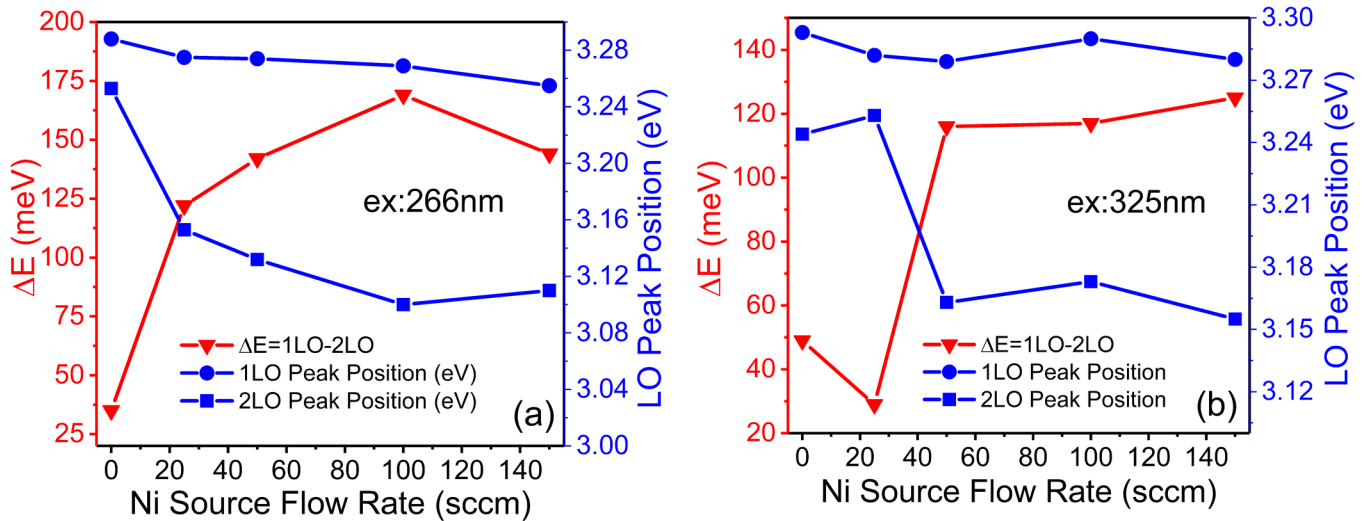


FIG. 5. Energy difference (red line) and energy value (blue line) diagrams with excitations of (a) 266 nm wavelength laser and (b) 325 nm wavelength laser, respectively.

incorporation of Ni^{2+} as substitutional sites (at least) in ZnO-Ni. Ni^{2+} is smaller than Zn^{2+} which could result in a reduced grain size of ZnO-Ni with Ni-doping.^{33,34} The grain size and strain are listed in Table I.

B. Optical characterization of ZnO-Ni

1. Room temperature PL

RT-PL spectra of MOCVD-grown ZnO-Ni samples are presented in Figs. 3(a) and 3(b). Two excitation wavelengths conditions of 266 nm and 325 nm lasers were used separately, and signals at different penetration depths were acquired. Figures 3(a) and 3(b) show spectra excited by 266 nm and 325 nm lasers, respectively, and scanned from 2.1 to 3.6 eV. Two luminescence bands with peaks at 3.3 and 2.6 eV are observed. With both the lasers' excitation wavelengths, the sample grown at a low Ni source flow rate (25 SCCM) shows the strongest luminescences, while the sample grown with the highest flow rate of 150 SCCM shows the weakest luminescences. The peak intensity of the near-band-edge emission at 3.3 eV of Ni25 is even higher than that of undoped ZnO and reduces as the Ni source flow rate is increased. Ni could form a nonradiative recombination center in ZnO, thereby reducing the luminescence intensities.³⁵ This is in accordance with the HRXRD results that the crystal quality of ZnO-Ni is better in samples with a lower Ni source flow rate. The proportion of the peak intensity at 2.6 eV relative to the near band-edge peak at 3.3 eV increases with Ni doping. No luminescence at 2.6 eV is observed in undoped ZnO. The broad peaks around 2.6 eV could be a result of defect states induced by Ni in the band structure of the host ZnO material. Ni doping with a high flow rate (≥ 50 SCCM) also introduces a secondary phase in the growth, suppresses interband transitions, and intensifies defects-related emission.^{24,35,36,37}

Figures 3(c) and 3(d) show enlarged views of the peaks after normalized intensity around 3.3 eV in Figs. 3(a) and 3(b). When processing the PL spectrum, the energy corresponding to the center of the Gauss emission peak at the near band edge (energy corresponding to the highest position of the peak) is usually considered as the bandgap.^{38–40} As seen in Fig. 3(c) (266 nm laser excitation), nickel doping systematically reduces the bandgap of ZnO from 3.289 to 3.255 eV. The variation of the bandgap with the doping flow rate in Fig. 3(d) (325 nm laser excitation) overall seems to follow a reducing trend from undoped to Ni-doped ZnO, but the trend with the Ni source flow rate is not as systematic as 266 nm laser excitation. The incorporation of Ni affects the structure of the material (grain size, strain) and regulates the energy band (emission peak) of the film. It forms shallow energy states and causes the bandgap to red-shift. The concentration of defect centers could vary with laser penetration depths which is reflected in Figs. 3(c) and 3(d).⁴¹ The penetration depth (D_p) can be estimated by the following formula:⁴²

$$D_p = \frac{\lambda}{4\pi k}, \quad (4)$$

where λ is the laser wavelength and k is extinction coefficient corresponding to the laser wavelength (266 nm: ~ 0.3 , 325 nm: ~ 0.25).⁴²

For the samples been discussed in this work, the thickness would range from 100 to 150 nm depending on the Ni flow rates with an average of 125 nm. 266 nm laser has a penetration depth of about 70 nanometers in ZnO, while 325 nm laser's penetration

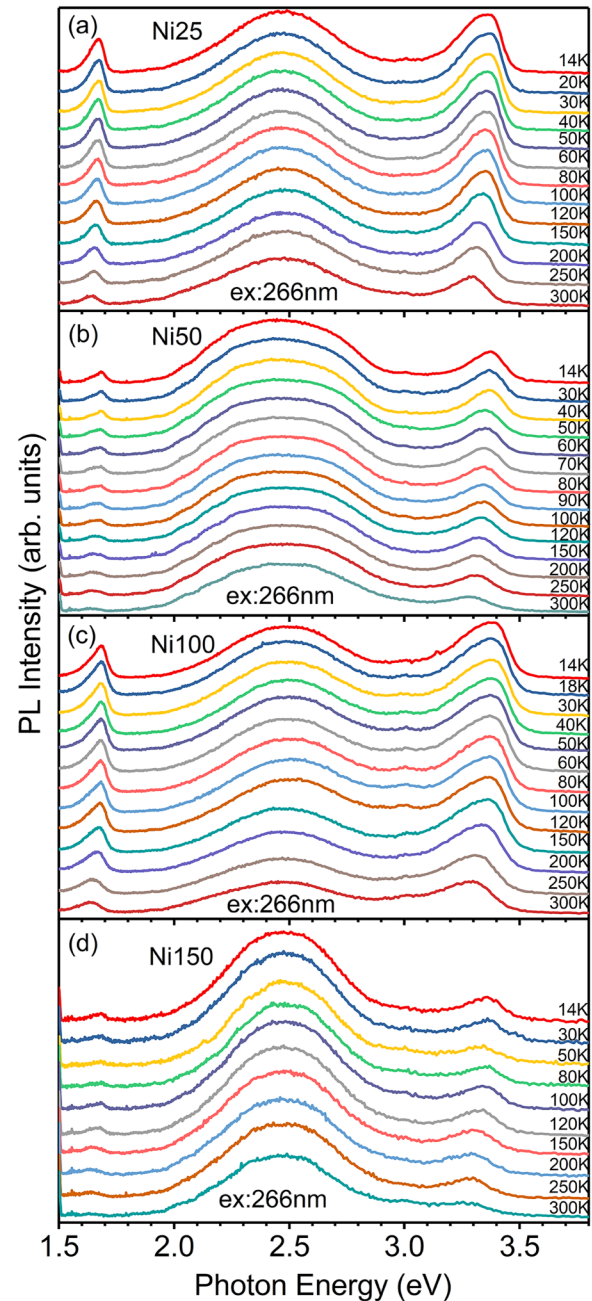


FIG. 6. (a)–(d) 266 nm wavelength laser excited temperature-dependent PL spectra of four ZnO-Ni samples.

depth is around 100 nm. Thus, the PL spectra show that the film has different luminescent properties in shallow (70 nm) and deep layers (100 nm). The bandgap overall reduced in Ni-doped ZnO as compared to un-doped ZnO in both the cases of laser excitation

wavelengths. These properties imply that Ni-induced defect states could be different at different penetration depths. The defect centers might not be very clearly identified as compared to the bulk, which could result in differences in the bandgap variation

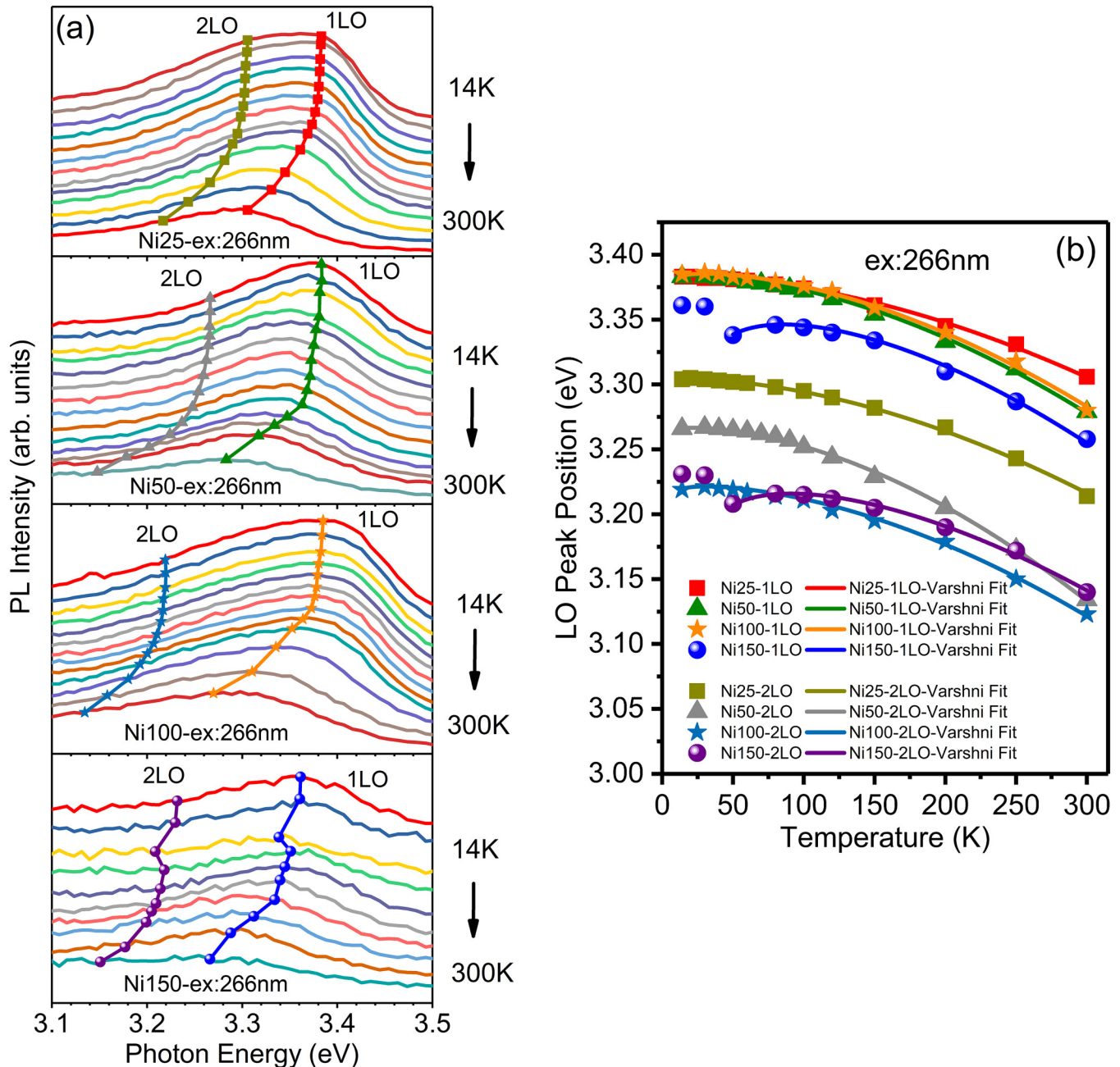


FIG. 7. (a) 1LO and 2LO peak position evolution from 14 to 300 K of four ZnO-Ni samples and (b) LO peak positions vs temperature and Varshni fits of LO peak positions for all ZnO-Ni samples.

with the Ni source flow rate with different excitation wavelengths. The distribution of Ni-induced defect states in the ZnO-Ni films is uneven along the growth direction. This is due to more defect centers, secondary phases, and agglomeration toward the surface. The Gaussian fitting of the band edge peak was performed for PL spectra excited by 266 and 325 nm laser as seen in Figs. 4(a) and 4(b). The band edge peak can be divided into two subpeaks, which can be signed as two different longitudinal optical (LO) phonon replicas from free excitons, named 1LO and 2LO. These two phonon peaks are very close in undoped ZnO, with an energy difference of about ~30 meV.³⁵ Ni doping separates these two phonon replica peaks up to ~120 meV as seen in the case of sample with the Ni source flow rate of 150 SCCM.

Figure 5 exhibits the energy difference and energy diagrams corresponding to the positions of the two phonon replica peaks, under two excitation of (a) 266 nm and (b) 325 nm, respectively. Overall trend looks similar under the two lasers' excitations. The peak position of two phonon replica modes is redshifted with an increase in nickel source flow rate, and the energy difference between the two phonon replica peaks increases. The trend is more defined in measurement with a lower penetration depth, as also seen in Fig. 3, due to a higher influence of Ni-doping toward the surface than the bulk.

2. Temperature-dependent photoluminescence (TD-PL)

Figures 6(a)–6(d) are 266 nm laser-excited TD-PL spectra of ZnO-Ni samples, with a temperature variation from 14 to 300 K and a spectral range from 1.5 to 3.8 eV. Three luminescence peaks are observed in the samples, at 3.26 eV (violet light), 2.5 eV (green light), and 1.63 eV (red light). As the temperature is lowered, a reduction in the scattering of photons by lattice vibrations increases PL emissions. The peak at 3.26 eV is the luminescence peak of the ZnO-Ni band edge, which blue-shifts with a decrease in temperature. The luminescence peak at 1.63 eV is a second-order peak of band edge emission (3.26 eV) and follows the same trend with temperature. The green emission peak at 2.5 eV is generally caused by defect-related luminescence, and does not shift with temperature. However, it could still be inter-related with the incorporation of Ni in ZnO-Ni. An increase in the 2.5 eV peak intensity with the increase of Ni source flow rate could partially be caused due to the increase in defect states introduced by Ni.

3. Bandgap-temperature properties

Figure 7 illustrates the peak splitting processes of PL band edge peaks, excited by 266 nm laser, with (a) for spectral variation versus temperature (T) and (b) for 1LO/2LO peak positions versus T and Varshni fits. Each band edge peak can be divided into two LO phonon replica peaks, 1LO and 2LO. Positions of these phonon replica peaks are red-shifted with an increase in the temperature as shown in Fig. 7(a). The red-shift is mainly caused by the electron-phonon interactions and the thermal expansion and contraction of crystal lattices.⁴³ The peak positions of two phonon replica peaks are plotted and fitted with the Varshni equation.^{44–46} As seen in Fig. 7(b), the bandgap shows a systematic blue shift with increasing temperature, which can be even better fitted after

TABLE II. Fitting parameters of the Varshni equation.

Sample	σ (meV)	α (1LO) (meV)	α (2LO) (meV)	β (K)	$E_g(0\text{ K})$ (1LO) (eV)	$E_g(0\text{ K})$ (2LO) (eV)
Ni25	0.6	2.21	2.50	2238	3.384	3.305
Ni50	1.7	3.01	3.79	2211	3.386	3.269
Ni100	2.5	2.89	2.82	2157	3.389	3.225
Ni150	12.3	3.08	2.60	2084	3.377	3.245

considering the carrier's localization.⁴⁷ A band-tail model⁴⁸ is applied to describe the localization states. In an inhomogeneous alloy system, the long-range order and periodicity of the crystal structure is broken, forming the band tail state. The band tail provides the energy levels to localize the carriers. As the temperature rises, carriers at these energy levels are thermally activated and migrate to shallow energy levels, which could increase the recombination energy. As the energy increase caused by such carrier migration exceeds the bandgap decrease caused by temperature rise, a blue-shift occurs in the spectrum.⁴⁷ The following fitting formula is applied for ZnO-Ni to understand the bandgap with respect to temperature:⁴⁷

$$E_g(k) = E_g(0\text{ K}) - \frac{\alpha^* T^2}{T + \beta} - \frac{\sigma^2}{k^* T}, \quad (5)$$

where $E_g(K)$ is the bandgap dependent on the temperature, $E_g(0\text{ K})$ is the bandgap at 0 K, k is the Boltzmann constant, T is the temperature, α , β are the Varshni parameters, σ is a factor to characterize

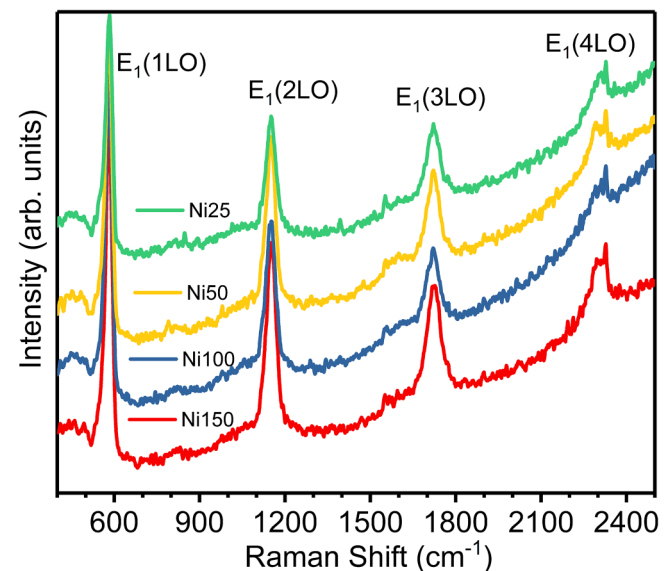


FIG. 8. Raman spectra of ZnO-Ni excited by 325 nm wavelength laser.

the inhomogeneity effect, value of this factor indicates the size of the inhomogeneity effect in the band-tail model.⁴⁸

Various parameters obtained by fitting are shown in Table II. α of 1LO ranges from 2.21 to 3.01 meV, the α value of 2LO is 2.50–3.79 meV, and the β value is around 2200 K. This β is close to the melting point of ZnO and decreases as the doping flow rate is increased. The $E_g(0\text{ K})(1\text{LO})$ value was almost consistent with varying Ni source flow rates; value of Ni150 was slightly lesser than the other three samples. The value of $E_g(0\text{ K})(2\text{LO})$ agrees well with the trend of the fitting result of the 2LO peak excited by 266 nm laser at normal temperature as shown in Fig. 5. Inhomogeneity factors from Ni25 to Ni150 range from 0.6 to 12.3 meV. When $\sigma = 12.3\text{ meV}$, a redshift-blueshift-redshift trend of peak position can be seen in Fig. 6(d). The dip in the blue shift trend at a temperature of about 50 K is due to anomalies that are caused when

phonons absorb energy to escape from inhomogeneity-related barriers to shallow energy levels.^{49,50}

C. Raman analysis

Figure 8 shows 325 nm laser-excited Raman spectra of the ZnO-Ni samples. Four peaks are seen at 584, 1168, 1752, and 2336 cm^{-1} , which are four frequency-multiplications of the LO phonon mode $E_1(\text{LO})$,^{27,43} called $E_1(1\text{LO})$, $E_1(2\text{LO})$, $E_1(3\text{LO})$, and $E_1(4\text{LO})$, respectively. These are typical resonant Raman peaks in ZnO based materials. Broad PL bands are observed in the high frequency region. 380 nm in PL corresponds to around 4400 cm^{-1} , and the FWHM of PL peak is observed as a background in Raman spectra starting at 1500 cm^{-1} , which complicates the data analysis in the high frequency region. The 1LO peak at the 584 cm^{-1} Raman shift is selected for data analysis, and this is the most defining peak for ZnO-Ni in general. Generally, the asymmetry of the Raman peak is due to a break in crystalline materials' translational symmetry at grain boundaries. This causes vibrational contributions from surfaces and interfaces, and formation of new phases that have spectral contributions.⁵¹ As also seen in HRXRD analysis, Ni-related phases were formed in ZnO-Ni along with a reduction in crystal grains' size and increase in grain boundaries, which could result in asymmetry in the Raman spectra.

Spectral asymmetry to the FWHM of Raman peaks is simplified for intuitive research, to understand the effect of nickel doping on the samples.^{52,53} This is related to the asymmetry (also related to doping) observed in the PL peaks at RT. As the accuracy of the Raman spectroscopy equipment is 0.2 cm^{-1} , asymmetry of the

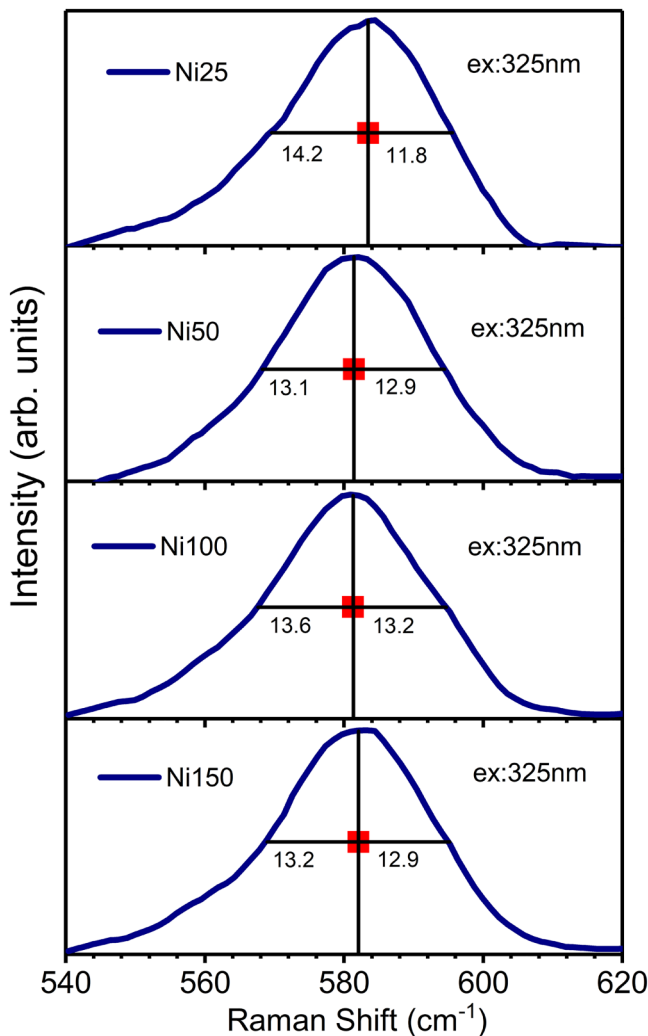


FIG. 9. Asymmetry of the Raman $E_1(1\text{LO})$ peak.

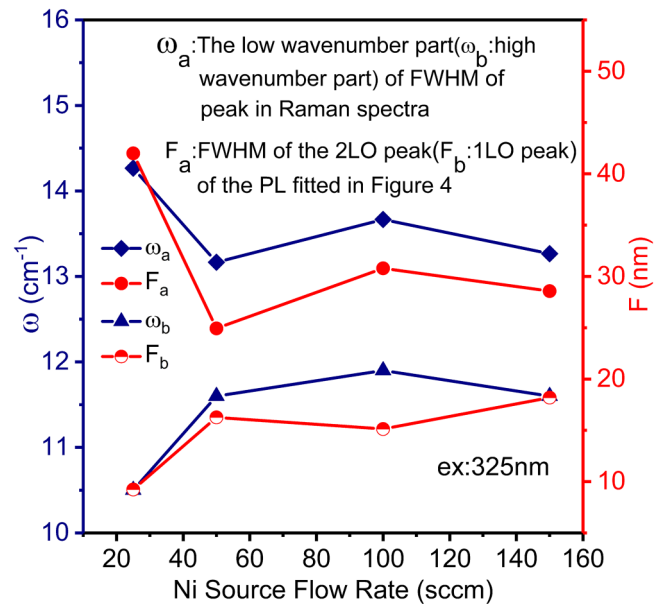


FIG. 10. Comparison based on the PL band-edge peak and Raman $E_1(1\text{LO})$ peak.

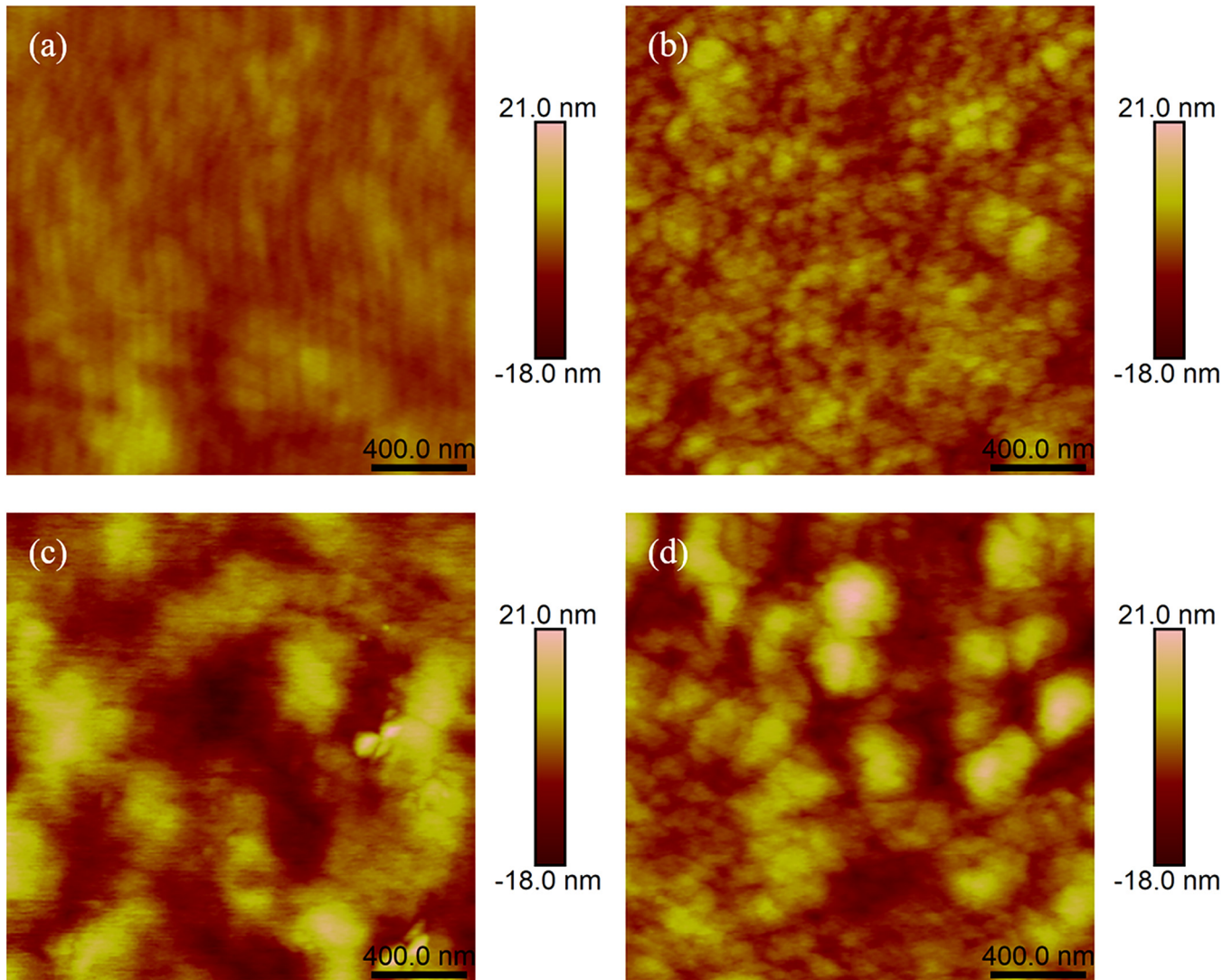


FIG. 11. $2 \times 2 \mu\text{m}$ AFM diagrams of four ZnO-Ni samples, (a) Ni25, (b) Ni50, (c) Ni100, and (d) Ni150.

Raman 1LO peak is represented by half of the FWHM as shown in Fig. 9. Variations in the two halves of asymmetric Raman peaks with Ni source flow rate are similar to the width of PL peaks excited by 325 nm laser, as seen in Fig. 10 (in which ω_a represents the low wavenumber part of FWHM of 1LO peaks in the Raman spectrum; ω_b represents the high wavenumber part of FWHM of 1LO peaks in the Raman spectrum, F_a represents FWHM of the 2LO peak of the PL fitted in Fig. 4, and F_b represents FWHM of the 1LO peak of the PL fitted in Fig. 4). Combining Raman and PL phonon replica modes and coupling effects, the LO modes of Raman and PL are proportionally related by constant associated with the data acquisition instrument.

D. Surface characterization of ZnO-Ni

1. Surface morphology characterization

AFM measurement was conducted to study the ZnO-Ni films surface morphology. $2 \times 2 \mu\text{m}$ micromorphology diagrams

TABLE III. Roughness of samples surfaces obtained by AFM.

Sample	Ni25	Ni50	Ni100	Ni150
Roughness (nm)	2.0	3.1	5.8	5.4

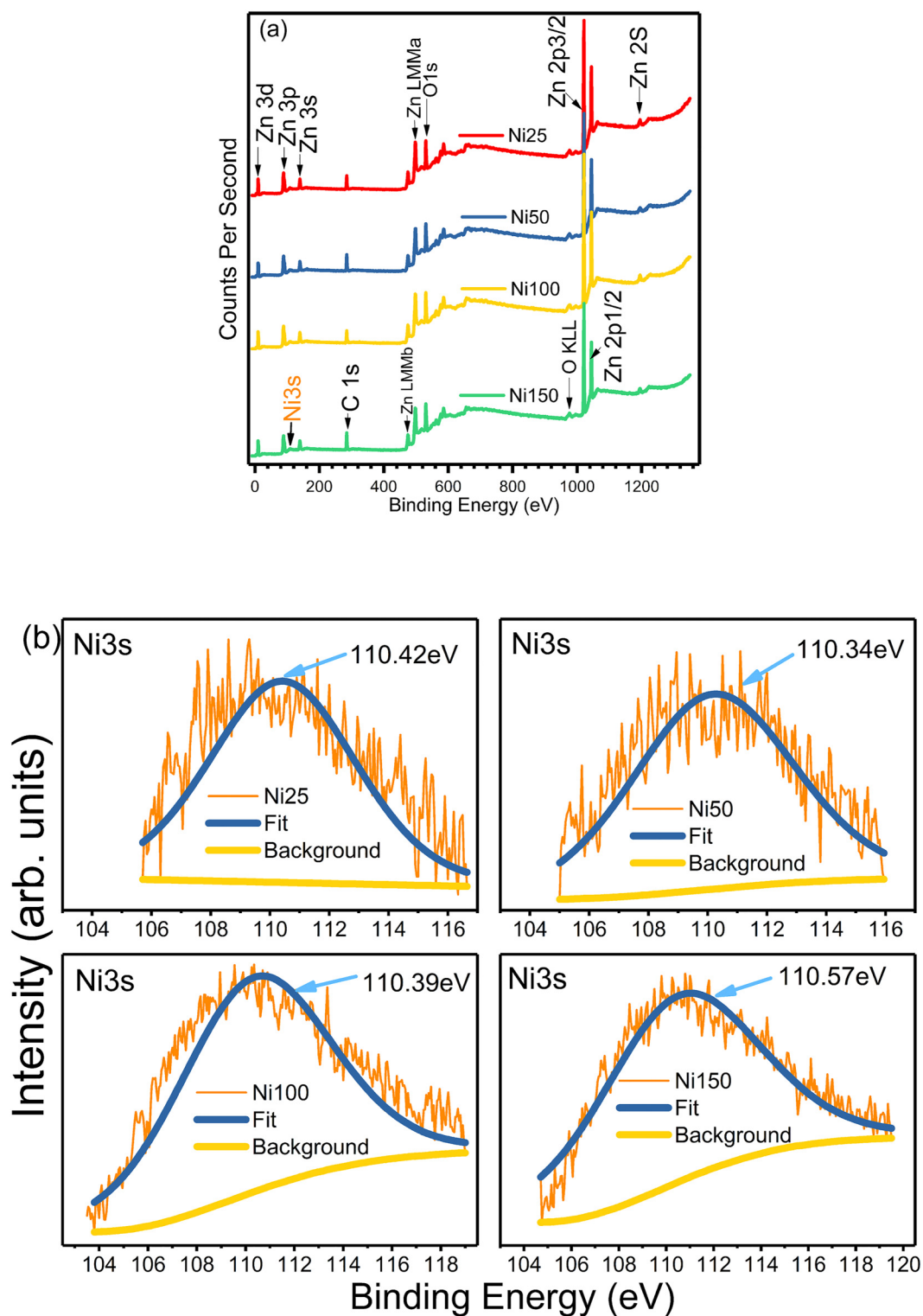


FIG. 12. (a) XPS wide-scan and (b) Ni3s fine scan of four ZnO-Ni samples.

TABLE IV. Ni3s peak parameters.

Sample	Ni25	Ni50	Ni100	Ni150
FWHM (eV)	5.82	6.43	7.36	7.88
Position (eV)	110.42	110.34	110.39	110.57

of the four samples surfaces are shown in Fig. 11. It can be seen that there are many granular fluctuations on the high Ni source flow rate sample surfaces (Ni100 and Ni150), which may be Ni particles deposited on the films. And, the surfaces of the samples doped with low source flow rates are relatively smooth. As shown in Table III, the surface roughness of the sample rises with Ni incorporation.

2. Chemical composition analysis

XPS spectra provide an important reference for the Ni content of the sample, which are indeed conducive to a more intuitive understanding of the effect of the Ni source flow rate on the Ni incorporation in the material. Wide-scan XPS spectra of four samples with different Ni source flow rates were obtained to study the surface elemental composition as shown in Fig. 12(a). Characteristic peaks including Zn (3d, 3p, 3s, LMMa&b, 2p3/2, 2p1/2, 2s), O1s, OKLL (Auger peak), C1s, and Ni3s were detected. Besides Zn, O, and Ni that from deposition sources, C was also detected, and the carbon peak may be caused by air or carbon-containing impurities adsorbed on the surface of samples.⁵⁴ The appearance of Ni3s peak indicates that the surface of the samples contains Ni element.⁵⁵ Fig. 12(b) shows the fine scans of Ni3s, the software XPSPEAK 4.1 was used to fit the XPS data. After using the Shirley iterative method to deal with the background, every XPS scan was fitted by a Gaussian-Lorentzian (20%–80%) function.⁵⁴ A peak of metallic Ni with binding energy of 110.3–110.6 eV was obtained, as shown in Table IV. Through the ratio of the peak areas of the fine scan spectra, we calculated the atomic ratio of the samples surface, and the results are listed in Table V. We obtained the atomic ratio of Ni component on the surface of four samples, 1.5%(Ni25), 2.2%(Ni50), 4.9%(Ni100), 7.7%(Ni150), respectively.

TABLE V. XPS analysis results of Ni element.

Sample	C1s (area/ SF)	N1s (area/ SF)	O1s (area/ SF)	Zn2p (area/ SF)	Ni3s (area/ SF)	Ratio of Ni (%)
Ni25	47 052	1287	53 394	45 503	2 266	1.5
Ni50	54 842	1532	49 540	38 771	3 181	2.2
Ni100	43 129	1479	55 746	46 720	7 708	4.9
Ni150	55 584	1562	50 929	37 632	12 271	7.7

IV. SUMMARY AND CONCLUSIONS

In summary, the material and optical properties of a series of ZnO-Ni films grown at varying Ni source flow rates by MOCVD are systematically studied. Crystal orientation in the (002) direction with a good crystal quality was observed in most ZnO-Ni samples. High Ni source flow rate results in secondary phases, deteriorates the crystal quality, and increases strain and dislocations. The bandgap of ZnO-Ni reduces with an increase in Ni source flow as per photoluminescence measurement. Also, a decrease in bandgap is seen with an increase in temperature. Ni incorporation results in a broad photoluminescence peak at 2.6 eV. This could be due to Ni-induced energy states possibly coupled with intrinsic O/Zn vacancies, interstitials, or antisites. ZnO-Ni samples with low Ni injection (25 sccm) exhibit enhanced luminescence as compared to undoped ZnO. However, higher Ni injection results in suppressed luminescence and more inhomogeneous defects-related luminescent centers. This increase in inhomogeneity with Ni-doping also results in asymmetries in crystal vibrations. This work demonstrates the effects of Ni doping on the structural and optical properties of ZnO grown by MOCVD and would contribute to the growth of ZnO-Ni films with high performances. This would help toward further investigation of ZnO-based materials for spintronic and optoelectronic applications.

ACKNOWLEDGMENTS

This work was supported by the National Natural Science Foundation of China (NNSFC) (No. 61367004), the Guangxi Natural Science Foundation (No. 2018GXNSFAA138127), and the State Key Laboratory of Luminescence and Applications (No. SKLA-2019-06).

DATA AVAILABILITY

The data that support the findings of this study are available from the corresponding author upon reasonable request.

REFERENCES

- ¹Zhe Chuan Feng, *Handbook of Zinc Oxides and Related Materials* (CRC, Taylor & Francis Group, London/New York, 2013), Vols. 1 and 2, pp. 440–640.
- ²William E. Fenwick, Matthew H. Kane, Zaili Fang, Tahir Zaidi, Nola Li, Varatharajan Rengarajan, Jeff Nause, and Ian T. Ferguson, *Mater. Res. Soc. Symp. Proc.* **957**, 410 (2006).
- ³S. K. Patil, S. S. Shinde, and K. Y. Rajpure, *Ceram. Int.* **39**, 3901 (2012).
- ⁴A. Smaali, S. Abdelli-Messaci, S. Lafane, A. Mavlonov, J. Lenzner, S. Richter, M. Kechouane, O. Nemraoui, and K. Ellmer, *Thin Solid Films* **700**, 137892 (2020).
- ⁵Sin-Liang Ou, Hong-Ru Liu, Shih-Yin Wang, and Dong-Sing Wu, *J. Alloys Compd.* **663**, 107 (2016).
- ⁶Yang Wang, Chuanle Zhou, Aline M. Elquist, Amirhossein Ghods, Vishal G. Saravade, Na Lu, and Ian Ferguson, *Proc. SPIE* **10533**, 105331R (2018).
- ⁷Shilpa Jain, Narayan Karmakar, Akshara Shah, and Navinchandra G. Shimpi, *Mater. Sci. Eng. B Adv.* **247**, 114381 (2019).
- ⁸L. M. Mahajan and D. S. Patil, *Mater. Res. Express* **6**, 076437 (2019).
- ⁹Teng Zhang, Zhen Xu, Jian Chen, Mingkai Li, Yinmei Lu, and Yunbin He, *J. Alloys Compd.* **833**, 155032 (2020).
- ¹⁰A. S. Kuz'mina, A. A. Lotin, N. A. Strokin, M. P. Kuz'min, and A. V. Kazantsev, *J. Cryst. Growth* **535**, 125506 (2020).

- ¹¹Naveen Kumar, Ashraful Haider Chowdhury, Behzad Bahrami, Mamun Reza Khan, Qiquan Qiao, and Mukesh Kumar, *Thin Solid Films* **700**, 137916 (2020).
- ¹²Amirhossein Ghods, Chuanle Zhou, and Ian T. Ferguson, *J. Vac. Sci. Technol. A* **38**, 042408 (2020).
- ¹³Amirhossein Ghods, Vishal G. Saravade, Chuanle Zhou, and Ian T. Ferguson, *J. Vac. Sci. Technol. A* **38**, 012406 (2020).
- ¹⁴B. Salameh, A. M. Alsmadi, and M. Shatnawi, *J. Alloys Compd.* **835**, 155287 (2020).
- ¹⁵Romain Tuyaerts, Jean-Pierre Raskin, and Joris Proost, *Thin Solid Films* **695**, 137760 (2020).
- ¹⁶V. Saravade, Z. Manzoor, A. Corda, C. Zhou, I. Ferguson, and N. Lu, *Proc. SPIE XVII*, 112881X (2020).
- ¹⁷Ashok Kumar Yadav, S. Maidul Haque, Rajnarayan De, Nimai Pathak, D. K. Shukla, R. J. Choudhary, D. M. Phase, S. N. Jha, and D. Bhattacharyya, *Thin Solid Films* **647**, 70 (2018).
- ¹⁸M. Sh Abdel-wahab, Asim Jilani, I. S. Yahia, and Attieh A. Al-Ghamdi, *Superlattices Microstruct.* **94**, 108 (2016).
- ¹⁹B. Babu, G. Rama Sundari, K. Ravindranadh, M. Rajesh Yadav, and R. V. S. S. N. Ravikumar, *J. Magn. Magn. Mater.* **372**, 79 (2014).
- ²⁰A. Mhamdi, B. Ouni, A. Amlouk, K. Boubaker, and M. Amlouk, *J. Alloys Compd.* **582**, 810 (2014).
- ²¹Md. R. Shakil, Abdelhamid M. El-Sawy, Habiba Tasnim, Andrew G. Meguerdichian, Jing Jin, Jacob P. Dubrosky, and Steven L. Suib, *Inorg. Chem.* **57**, 9977 (2018).
- ²²Chandrasekaran Abinaya, Thibeorchews Prasankumar, Sujin P Jose, Kandasamy Anitha, Craig Ekstrum, Joshua M. Pearce, and Jeyanthinath Mayandi, *Chem. Select* **2**, 9014 (2017).
- ²³Kun Xu, Changzhen Liu, Rui Chen, Xiaoxiang Fang, Xiuling Wu, and Jie Liu, *Phys. B* **502**, 155 (2016).
- ²⁴Samarpita Senapati, Suneel K. Srivastava, and Shiv B. Singh, *Nanoscale* **4**, 6604 (2012).
- ²⁵P. R. Chithira and Teny Theresa John, *J. Alloys Compd.* **766**, 572 (2018).
- ²⁶A. P. Rambua, L. Ursu, N. Iftimie, V. Nica, M. Dobromir, and F. Iacomì, *Appl. Surf. Sci.* **280**, 598 (2013).
- ²⁷Demet İskenderoğlu and Harun Güney, *Ceram. Int.* **43**, 16593 (2017).
- ²⁸I. Neelakanta Reddy, Ch. Venkata Reddy, Jaesool Shim, Bhargav Akkinapally, Migyung Cho, Kisoo Yoo, and Dongseob Kim, *Catal. Today* **340**, 277 (2020).
- ²⁹K. D. Rogers and P. Daniels, *Biomaterials* **23**, 2577 (2002).
- ³⁰G. K. Williamson and W. H. Hall, *Acta Metall.* **1**, 22 (1953).
- ³¹A. Khorsand Zak, W. H. Abd, Majid, M. E. Abrishami, and Ramin Yousefi, *Solid State Sci.* **13**, 251 (2011).
- ³²Josef Ellingsen, Vishnukanthan Venkatachalapathy, Alexander Azarov, Ola Nilsen, and Andrej Kuznetsov, *Thin Solid Films* **709**, 138245 (2020).
- ³³H. Ali, A. M. Alsmadi, B. Salameh, M. Mathai, M. Shatnawi, N. M. A. Hadia, and E. M. M. Ibrahim, *J. Alloys Compd.* **816**, 152538 (2019).
- ³⁴Gunjan Srinet, Ravindra Kumar, and Vivek Sajal, *J. Appl. Phys.* **114**, 033912 (2013).
- ³⁵Oscar Marin, Patricio Alastuey, Ezequiel Tosi, Joseba Orive, Edgar Mosquera, Guillermo Zampieri, Sergio Suárez, David Comedi, and Mónica Tirado, *Appl. Surf. Sci.* **456**, 771 (2018).
- ³⁶K. P. Shinde, R. C. Pawar, B. B. Sinha, H. S. Kim, S. S. Oh, and K. C. Chung, *Ceram. Int.* **40**, 16799 (2014).
- ³⁷Jin Wang, Xin Dong, Baolin Zhang, Yuantao Zhang, Hui Wang, Zhifeng Shi, Shikai Zhang, Wei Yin, and Guotong Du, *J. Alloys Compd.* **579**, 160 (2013).
- ³⁸L. Cabral, Victor Lopez-Richard, Juarez L. F. Da Silva, G. E. Marques, Matheus P. Lima, Y. J. Onofre, M. D. Teodoro, and M. P. F. de Godoy, *J. Lumin.* **227**, 117536 (2020).
- ³⁹Liping Fang, Haolin Li, Xuhang Ma, Qiuming Song, and Rui Chen, *Appl. Surf. Sci.* **527**, 146818 (2020).
- ⁴⁰L. El Mir, A. Amlouk, C. Barthou, and S. Alaya, *Physica B* **388**, 412 (2007).
- ⁴¹Perry C. Grant *et al.*, *Nanotechnology* **29**, 465201 (2018).
- ⁴²S. Rajeh, A. Mhamdi, K. Khirouni, M. Amlouk, and S. Guermazi, *Opt. Lasers Technol.* **69**, 113 (2015).
- ⁴³R. P. Wang, G. Xu, and P. Jin, *Phys. Rev. B* **69**, 113303 (2004).
- ⁴⁴Soaram Kim *et al.*, *Bull. Korean Chem. Soc.* **34**, 3335 (2013).
- ⁴⁵Giwoong Nam, Hyunggil Park, Hyunsik Yoon, Jong Su Kim, and Jae-Young Leem, *Curr. Appl. Phys.* **13**, S168 (2013).
- ⁴⁶Qianhui Yang, Liren Lou, and Guanzhong Wang, *Phys. E* **89**, 124 (2017).
- ⁴⁷W. Liu *et al.*, *J. Alloys Compd.* **625**, 266 (2015).
- ⁴⁸Petr G. Eliseev, Marek Osinski, Jinhyun Lee, Tomoya Sugahara, and Shiro Sakai, *J. Electron. Mater.* **29**, 332 (2000).
- ⁴⁹Yong-Hoon Cho, G. H. Gainer, A. J. Fischer, J. J. Song, S. Keller, U. K. Mishra, and S. P. DenBaars, *Appl. Phys. Lett.* **73**, 1370 (1998).
- ⁵⁰W. Liu *et al.*, *Opt. Express* **23**, 15935 (2015).
- ⁵¹Gwénaél Gouadec and Philippe Colomban, *Prog. Cryst. Growth Charact. Mater.* **53**, 1 (2007).
- ⁵²Rajesh Kumar, Gayatri Sahu, Shailendra K. Saxena, Hari M. Rai, and Pankaj R. Sagdeo, *Silicon* **6**, 117 (2014).
- ⁵³Shuai Chen, Lingyu Wan, Deng Xie, Zhi Ren Qiu, Xiaodong Jiang, Chin-Che Tin, and Zhe Chuan Feng, *J. Phys. D: Appl. Phys.* **50**, 115102 (2017).
- ⁵⁴Hong Yang *et al.*, *Appl. Surf. Sci.* **479**, 1246 (2019).
- ⁵⁵A. G. Kochur, T. M. Ivanova, S. J. Hinder, J. F. Watts, A. A. Sidorov, M. A. Kiskin, V. M. Novotortsev, and I. L. Eremanenko, *J. Electron. Spectrosc.* **184**, 501 (2011).